

# Leaky Mode Resonance-Induced Sensitive Ultraviolet Photodetector Composed of Graphene/Small Diameter Silicon Nanowire Array Heterojunctions

Jun-Jie Wang, Can Fu, Hai-Yang Cheng, Xiao-Wei Tong, Zhi-Xiang Zhang, Di Wu, Li-Miao Chen, Feng-Xia Liang,\* and Lin-Bao Luo\*



Cite This: *ACS Nano* 2021, 15, 16729–16737



Read Online

ACCESS |



Metrics & More



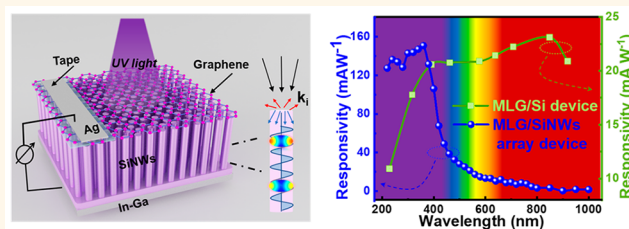
Article Recommendations



Supporting Information

**ABSTRACT:** Ultraviolet photodetectors (UVPDs) based on wide band gap semiconductors (WBSs) are important for various civil and military applications. However, the relatively harsh preparation conditions and the high cost are unfavorable for commercialization. In this work, we proposed a non-WBS UVPD by using a silicon nanowire (SiNW) array with a diameter of 45 nm as building blocks. Device analysis revealed that the small diameter SiNW array covered with monolayer graphene was sensitive to UV light but insensitive to both visible and infrared light illumination, with a typical rejection ratio of 25. Specifically, the responsivity, specific detectivity, and external quantum efficiency under 365 nm illumination were estimated to be 0.151 A/W,  $1.37 \times 10^{12}$  Jones, and 62%, respectively, which are comparable to or even better than other WBS UVPDs. Such an abnormal photoelectrical characteristic is related to the  $\text{HE}_{1m}$  leaky mode resonance (LMR), which is able to shift the peak absorption spectrum from near-infrared to UV regions. It is also revealed that this LMR is highly dependent on the diameter and the period of the SiNW array. These results show narrow band gap semiconductor nanostructures as promising building blocks for the assembly of sensitive UV photodetectors, which are very important for various optoelectronic devices and systems.

**KEYWORDS:** wide band gap semiconductors, ultraviolet photodetector, silicon nanowire array, leaky mode resonance, narrow band gap semiconductors



Ultraviolet photodetectors (UVPDs) have attracted extensive attention due to their promising applications in environmental monitoring, biological and chemical analysis, flame detection, and Internet of Things sensors.<sup>1–3</sup> For example, UVPD chips have been widely used in wearable devices, weather stations, and other optoelectronic systems to monitor outdoor UV intensity.<sup>4,5</sup> In addition, in the fields of disinfection and sterilization, water quality detection, and coating curing, UVPDs are indispensable tools to monitor the radiation dose.<sup>6</sup> With the rapid advances in semiconductor technology, the past decade has witnessed the development of various high-performance UVPDs based on different wide band gap semiconductors (WBSs), including SiC,<sup>7</sup> GaN,<sup>8</sup> ZnO,<sup>9</sup> Ga<sub>2</sub>O<sub>3</sub>,<sup>10</sup> etc. These WBS-based UVPDs indeed possess excellent performance such as high responsivity, low dark current, good sensitivity, high UV/vis rejection ratio, and satisfying ambient stability.<sup>11</sup> However, these WBS-based UVPDs have their own unavoidable shortcomings. For

instance, the response time of these conventional UVPDs is limited by the high surface state/defects,<sup>12</sup> hindering their practical application in high-speed UV detection. In addition, the above inorganic WBSs are mainly grown by physical vapor transport (PVT),<sup>13</sup> molecular beam epitaxy (MBE),<sup>14</sup> metal–organic chemical vapor deposition (MOCVD),<sup>15</sup> and metal–organic vapor phase epitaxy (MOVPE),<sup>16</sup> which means that the preparation conditions are harsh, leading to relatively high fabrication costs.<sup>17</sup> From the perspective of material growth and photoelectric properties, silicon is an ideal material for light detection owing to its relatively low cost, mature

**Received:** August 5, 2021

**Accepted:** September 30, 2021

**Published:** October 4, 2021



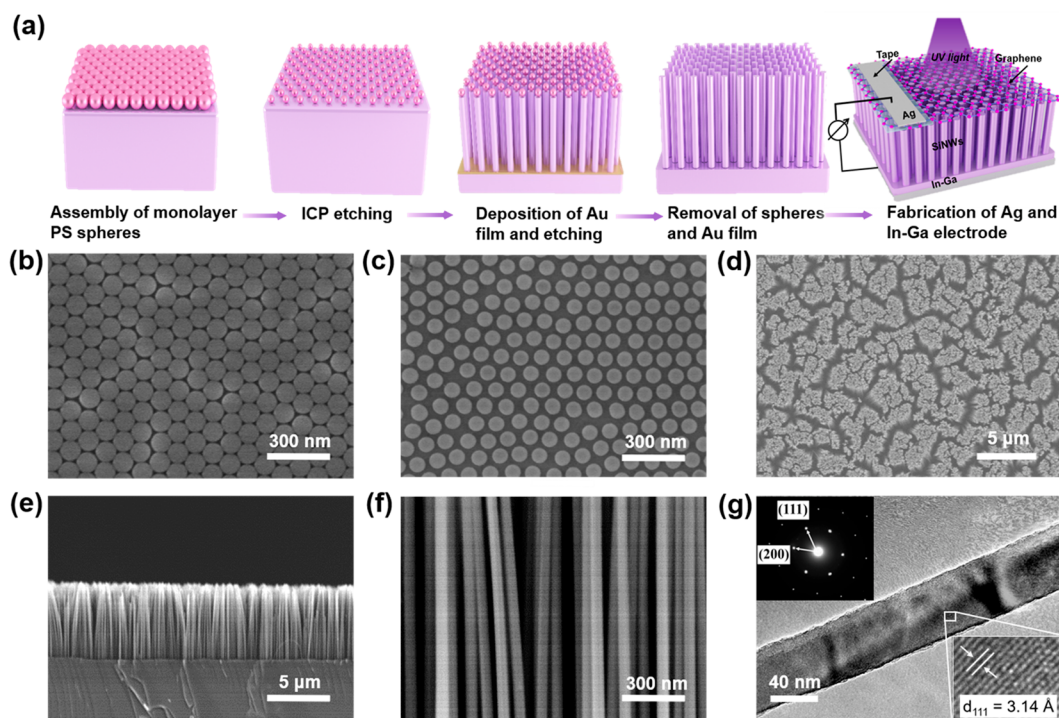


**Figure 1.** (a) Flowchart for fabricating MLG/SiNW array heterojunction UVPD. (b) SEM image of hexagonal closely stacked PS spheres. (c) SEM image of size-reduced PS spheres after ICP etching. (d) Top- and (e) side-view SEM images of the SiNW array. (f) High-magnification side-view SEM image. (g) HRTEM image of SiNW. The inset shows the corresponding lattice structure and SAED pattern.

manufacturing process, and fast response speed.<sup>18</sup> Unfortunately, the majority of Si-based photodetectors show strong sensitivity to visible and near-infrared (NIR) light irradiation, but relatively weak sensitivity to UV light due to their narrow band gap.<sup>19</sup> To achieve UV light detection, additional filters are often equipped onto silicon-based photodetectors to block visible and infrared photons, which undoubtedly leads to increased fabrication cost and complexity.<sup>20</sup>

A variety of studies have shown that illuminating semiconductor nanostructures with subwavelength diameters can induce different leaky mode resonances (LMRs), including TM (transverse magnetic,  $H_z = 0$ ), TE (transverse electric,  $E_z = 0$ ), HE (magnetoelectric, TM-like), and EH (electromagnetic, TE-like).<sup>21–24</sup> These LMRs can selectively enhance the optical absorption in a particular spectral region, which facilitates the tailoring of related optical absorption properties. For example, Cao *et al.* reported that, based on the LMR-induced field enhancement theory, the fundamental absorption properties of germanium nanostructures can be spectrally tuned from 1200 to 600 nm by reducing their diameter from 220 to 20 nm.<sup>23</sup> In addition, by using numerical simulation and optical waveguide theory, Leu's group theoretically predicted that silicon nanostructures can exhibit tunable and selective resonance absorption, according to which the corresponding absorption peak could be shifted from NIR light to visible light by engineering the diameter of the nanostructure from 120 to 70 nm.<sup>24</sup> Inspired by the above work, herein, we proposed a sensitive UVPD by choosing subwavelength diameter silicon nanowires (SiNWs) as building blocks. Both experimental results and theoretical simulations based on the finite element method (FEM) reveal that the SiNW array with an average diameter of  $\sim 45$  nm fabricated by the metal-assisted chemical etching method shows peak absorption in the UV region. Such a finding is different from previously reported SiNWs with

relatively large diameters and can be attributed to the leaky mode resonance of the small dimension. Further device analysis revealed that the SiNW array covered with a graphene layer is sensitive to UV light but nearly insensitive to both visible and NIR light illumination. The corresponding responsivity, specific detectivity, and external quantum efficiency are comparable to or even better than those of other UVPDs made of conventional WBSs. In light of the simple manufacturing process and relatively good device performance, we believe this work will provide an effective method for low-cost silicon-based UVPDs without additional filters.

## RESULTS AND DISCUSSION

Figure 1a shows the stepwise fabrication of the UVPD which is composed of a subwavelength diameter SiNW array covered with graphene. In addition, the Ag paste electrode was coated onto graphene on insulating tape, and the In-Ga alloy electrode was pasted onto the silicon substrate to form an ohmic contact (Figure S1a,b). During the device fabrication process, the SiNW array was synthesized by metal-assisted chemical etching (MCE),<sup>25,26</sup> in which Si loaded with a patterned Au film was immersed into a mixed etching solution ( $\text{HF:H}_2\text{O}_2 = 4:1$  (v/v)). Moreover, monolayer graphene (MLG) films were grown by a chemical vapor deposition (CVD) method.<sup>27</sup> Scanning electron microscopy (SEM) images revealed that all the PS spheres were uniformly and densely distributed on the silicon wafer in a hexagonal close packing manner (Figure 1b). The PS spheres were then thinned down by inductively coupled plasma (ICP) etching to form a non-close-packed pattern, as displayed in Figure 1c. After deposition of gold thin film ( $\sim 25$  nm) by sputtering, the sample was immersed in an etching solution, in which selective etching was catalyzed by the gold film. Figure 1d–f shows SEM images of the as-etched product

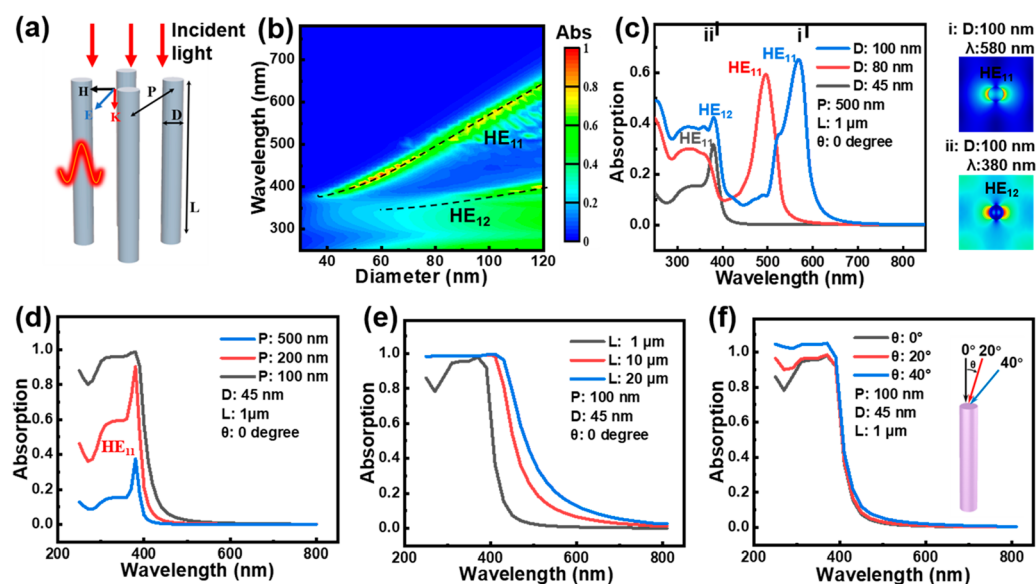


**Figure 2.** (a) Schematic illustration of the vertical SiNW array. (b) Contour plot of the absorption (Abs) as a function of wavelength and SiNW diameter ( $D$ ). (c) Simulations of the absorption spectrum of SiNWs with diameters of 100, 80, and 45 nm. The inset shows the electric field intensity at  $\lambda = 580$  and 380 nm for a diameter of 100 nm, corresponding to the  $HE_{11}$  and  $HE_{12}$  modes, respectively. (d) The effect of the period on the absorption spectrum. (e) The influence of SiNW length ( $L$ ) on the absorption spectrum. (f) The influence of the incident angle on the absorption spectrum.

at different magnifications. The SiNW array has a uniform length of  $\sim 6.7 \pm 0.3 \mu\text{m}$ . Further high-resolution transmission electron microscopy (HRTEM) image and selected area electron diffraction (SAED) pattern in Figure 1g show that the as-etched SiNW has a smooth surface, with typical single-crystal characteristics. According to the statistical diameter distribution of the scraped NWs in Figure S2a,b, the average diameter of the SiNW array is approximately  $45 \pm 5$  nm. The Raman spectrum of the graphene film in Figure S3 shows a weak D-band peak and intensity ratio ( $I_{2D}/I_G$ ) of approximately  $\approx 2.9$ , indicative of good quality and monolayer properties of the graphene. In addition, the relatively low sheet resistance (approximately 300 Ohm/sq) can facilitate the transport of carriers during the UV detection process.

Undoubtedly, the diameter of the above SiNW array is far from the exciton Bohr radius, which means that it is impossible to induce any quantum effect. However, the relatively small diameter can induce an obvious shift of peak absorption from NIR to UV light, according to theoretical simulation by numerically solving Maxwell's equations (see Supporting Information (SI)). Figure 2a shows a diagram of the vertical SiNWs array. By setting the parameters of period ( $P = 500$  nm) and length ( $L = 1 \mu\text{m}$ ), a contour map of the dependence of light absorption on the diameter and wavelength is plotted in Figure 2b. The optical absorption of SiNWs shows two different branches. The peak absorption due to the  $HE_{11}$  (magnetoelectric, TM-like) leaky mode resonance is found to shift to short wavelengths when the diameter decreases from 120 to 40 nm. Meanwhile, the absorption attributable to the  $HE_{12}$  leaky mode resonance begins to gradually weaken, and a very weak shift from 390 to 360 nm is observed when the diameter of the SiNWs gradually decreases from 120 to 60 nm, leading to distinct optical absorption for different diameters of SiNWs. Such a shift of  $HE_{11}$  and  $HE_{12}$  to short wavelengths with decreasing diameter is understandable as the coupling between light and leaky modes is highly dependent on the diameter of the NW, according to the solution of Maxwell's

equation (please see the SI for more details). As shown in Figure 2c, the simulated absorption curve for 100 nm SiNWs is characterized by two peaks (580 nm due to  $HE_{11}$  and 380 nm due to  $HE_{12}$ ), which is consistent with previously reported results.<sup>28</sup> However, the absorption is composed of only one peak located at 380 nm when the diameter of SiNW is decreased to 45 nm. When the diameter decreases gradually from 40 to 30 nm, the peak absorption due to  $HE_{11}$  is found to slightly shift from 370 to 360 nm (Figure S4). Meanwhile, the intensity is very low, which means that the enhancement in absorption due to  $HE_{11}$  is relatively weak. Further simulation results disclose that the optical absorption is highly dependent on the period and length of the SiNW array, and the illumination angle (Figure S5). Figure 2d exhibits the absorption curve of 45 nm SiNWs with different periods (500, 200, and 100 nm). It is clear that a decrease in period can bring about an enhanced and broadened absorption spectrum in the UV region, due to strengthened internanowire coupling for the high-density SiNW array. Moreover, the length of the SiNWs can also affect the absorption spectrum. Figure 2e shows the absorption curve of the SiNW array as a function of different wavelengths, according to which SiNWs with relatively large lengths tend to absorb longer wavelengths of illumination in that the penetration depth of Si is highly dependent on the wavelengths of incident light. Further simulation results show that an incident angle between  $0^\circ$  and  $40^\circ$  can hardly influence the absorption spectrum (Figure 2f), which should be caused by the weakening of the dependence on the incident angle by the high-density SiNW array.<sup>29</sup>

To gain more insight into the absorption enhancement of the SiNW array in the UV region, the electric field of the SiNW array with a diameter of 45 nm, a period of 100 nm, and a length of  $1 \mu\text{m}$  under various light illumination conditions was further simulated. A comparison of the electric field distribution of SiNW arrays on the  $x$ - $y$  and  $x$ - $z$  planes finds that only irradiation with 365 nm light can induce a relatively strong electric field inside the SiNW (Figure 3a,b). In addition,



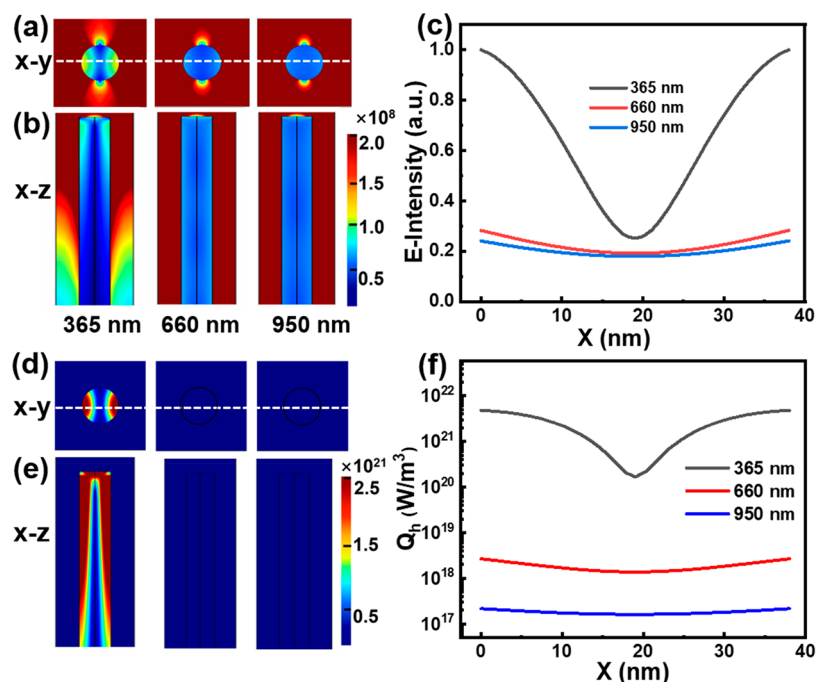


Figure 3. Electric field distribution of the SiNW array in the (a)  $x$ -y and (b)  $y$ -z planes excited by illumination with wavelengths of 365, 660, and 950 nm, respectively. (c) Electric intensities corresponding to dashed lines' positions of SiNW shown in (a). The total power loss density plots in the (d)  $x$ -y and (e)  $x$ -z planes excited by illumination with wavelengths of 365, 660, and 950 nm, respectively. (f) Total power loss density corresponding to dashed lines' positions in (d). The simulation parameters of the SiNW array are  $D = 45$  nm,  $P = 100$  nm,  $L = 1$   $\mu$ m, and  $\theta = 0^\circ$ .

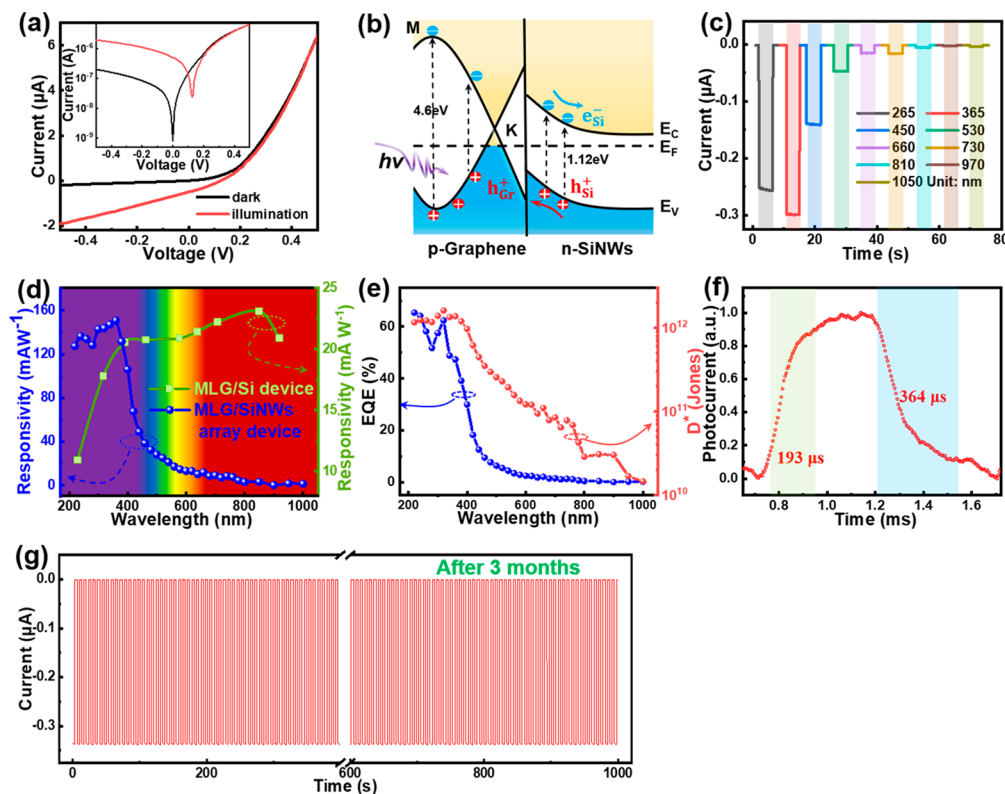


Figure 4. (a)  $I$ - $V$  curves of the MLG/SiNW array heterojunction UVPD in the dark and under 365 nm illumination with an intensity of  $1.469$   $\text{mW cm}^{-2}$ ; the inset shows the corresponding log  $I$ - $V$  curves. (b) Energy band diagram of the MLG/SiNWs UVPD. (c) Photoresponse of the device under different illuminations ( $0.5$   $\text{mW cm}^{-2}$ ). (d) Comparison of the responsivity of the present MLG/SiNW array and MLG/Si wafer heterojunction photodetector. (e) The external quantum efficiency and specific detectivity of the UVPD as a function of wavelength at  $0$  V. (f) A single normalized cycle of the device for estimating both rise time and fall time. (g) Photoresponse of the UVPD for approximately 60 cycles of operation before and after storage for 3 months.

**Table 1.** Comparison of the Performance Parameters of the Present and Other WBS-Based and Commercial UVPDs

photodetector	device type <sup>a</sup>	wavelength [nm]@bias [V]	R [mA/W]	$\tau$ [ $\mu$ s]	$D^*$ [Jones]	ref
MLG/SiNWs array	Schottky	365@0	151	193	$1.37 \times 10^{12}$	this work
TiO <sub>2</sub> /WO <sub>3</sub>	PC	382	48.13		$9.76 \times 10^{10}$	39
ZnO/SnO <sub>2</sub> core-shell nanorod arrays	Schottky	365@1	$2.85 \times 10^4$	$8.7 \times 10^6$	$2.9 \times 10^{14}$	40
WO <sub>3</sub>	PC	382	1002	$5.3 \times 10^5$	$2.088 \times 10^{12}$	41
WO <sub>3</sub>	PC	382	940		$1.97 \times 10^{12}$	42
WO <sub>3</sub> /graphene	PC	382@3	253		$5.136 \times 10^{11}$	43
Li <sub>0.2</sub> Ni <sub>0.8</sub> O	PC	382	218		$4.67 \times 10^{11}$	44
$\beta$ -Ga <sub>2</sub> O <sub>3</sub> micro/nanosheet	Schottky	254@1	$1.931 \times 10^4$	$<2 \times 10^4$		45
Ag/ZnO/Ag	M-S-M	365@5	$2.814 \times 10^4$	$9 \times 10^6$		46
nonpolar GaN	Schottky	325@0.05	12	$2.8 \times 10^5$	$6.07 \times 10^8$	47
Ni/GaN/Ti/Al	Schottky	360@0	104	$1 \times 10^4$		48
ZnO NW array/Spiro-MeOTAD	Schottky	390@0	17	950		49
GaN (GUVA-S12SD in Gen UV)	Schottky	350@0.1	140	$10^4$		

<sup>a</sup>PC and M-S-M represent photoconductive and metal-semiconductor-metal structures, respectively.

by extracting the electric field intensity at the dotted line in Figure 3a, one can see that, for most of the area, the intensity of the trapped electric field within the SiNWs under 365 nm illumination is much larger than that of other wavelengths (Figure 3c). In fact, this finding is also confirmed by the simulated total power loss density distribution and value of different wavelengths. As shown in Figure 3d–f, the loss of photon energy ( $Q_i$ ) under 365 nm light in SiNWs is much more severe than that at other illumination wavelengths. Since in this case, the intrinsic absorption constitutes the main reason for the photon energy loss,<sup>30</sup> the majority of incident UV photons will be absorbed by the SiNWs, which might be beneficial for UV light detection. It should be noted that, while a number of research groups have reported various SiNW arrays that exhibit tailorable absorption in the NIR and visible light regions,<sup>31,32</sup> we have successfully reported experimentally SiNW arrays whose peak absorption can be tuned from the NIR to UV light regions by engineering the diameter. This finding is interesting and can be attributed to the PS assisted etching method, which can achieve very good anisotropic Si etching with aspect ratios as high as 100.

Similar to other graphene/semiconductor heterojunctions,<sup>33</sup> the current monolayer graphene (MLG)/SiNW array heterojunction exhibits a typical rectifying effect with a rectification ratio of  $\sim 30$  at  $\pm 0.5$  V as shown in Figure 4a. Furthermore, when illumination with 365 nm light (light intensity of  $1.469 \text{ mW cm}^{-2}$ ), the MLG/SiNW device will show a pronounced photovoltaic effect, with a  $V_{oc}$  and  $J_{sc}$  of 0.13 V and  $0.5 \mu\text{A}$ , respectively. From the perspective of solar cell application, the energy conversion efficiency ( $\sim 0.51\%$ ) is not competitive in comparison with previously reported graphene photovoltaic devices.<sup>34</sup> However, the current ratio ( $I_{\text{photocurrent}}/I_{\text{darkcurrent}}$ ) at 0 V is as high as  $\sim 600$ , suggesting that the MLG/SiNW array heterojunction could act as a sensitive UVPD without a power supply. The working mechanism of this self-driven UVPD can be explained by the energy band diagram shown in Figure 4b. Once the weak *p*-type MLG caused by the doping of oxygen and water vapor in the air is in contact with Si,<sup>35</sup> electrons will diffuse from Si to MLG while the holes diffuse from MLG to Si due to the difference in the work function. As a result, the energy levels near the Si surface will bend upward, forming a built-in electric field at the interface with a direction pointing from Si to MLG. Once illumination by UV light, UV photons will be absorbed by the MLG/SiNW device due to the reason mentioned above and the resultant photogenerated electron-

hole pairs (EHPs) will be separated in the depletion region, forming a photocurrent in the circuit. Note that, during this photoelectric process, the majority of the photogenerated EHPs will be separated without recombination due to the good quality of the MLG/SiNW interface. As a consequence, the photocurrent is found to increase linearly with increasing light intensity (Figure S6).

Further device analysis reveals that, in addition to the obvious photoresponse to 365 nm, our MLG/SiNW heterojunction UVPD is also sensitive to 265 nm deep ultraviolet (DUV) illumination (Figure 4c). Nevertheless, as the illumination was further switched to longer wavelengths such as visible and even NIR light, the sensitivity was weak, consistent with the corresponding responsivity ( $R$ ), specific detectivity ( $D^*$ ), and external quantum efficiency ( $EQE$ ) in the region from 200 to 1000 nm (Figure 4d,e). This special spectral selectivity with peak sensitivity in the UV region is in sharp contrast with previously reported silicon nanostructure-based PDs, including Ti/SiNW array/Au,<sup>36</sup> graphene/SiNWs with random diameters,<sup>37</sup> hourglass shaped SiNWs,<sup>38</sup> and even graphene/planar Si wafer devices, whose maximum sensitivities are all located at approximately 1000 nm (Figure 4d), corresponding to the intrinsic band gap of Si. Specifically, the maximum  $R$ ,  $D^*$ , and  $EQE$  of the present MLG/SiNW heterojunction device are calculated to be  $0.151 \text{ A/W}^{-1}$ , 62%, and  $1.37 \times 10^{12}$  Jones at a bias of 0 V (see SI for details), respectively. By deducing an individual cycle of photoresponse, the rise/fall time of the MLG/SiNW array UVPD is estimated to be 193/364  $\mu\text{s}$ , which is relatively slow in comparison with that of previously reported silicon-based devices (Figure 4f). Such a slow photoresponse is probably due to the relatively poor graphene/SiNW contact after the removal of PMMA. In addition, the present UVPD also exhibits excellent ambient stability. Even after 3 months of storage in an ambient environment, the device does not exhibit any degradation in the photocurrent (Figure 4g), which should be attributed to the excellent stability of both the graphene and the SiNW array. Table 1 compares the representative device parameters ( $R$ ,  $\tau$ , and  $D^*$ ) of the MLG/SiNW array device and other UVPDs made of conventional WBSs. Obviously, these parameters are poorer than those of WBS UVPDs composed of metal oxide semiconductors such as TiO<sub>2</sub>,<sup>39</sup> SnO<sub>2</sub>,<sup>40</sup> WO<sub>3</sub>,<sup>41–43</sup> NiO,<sup>44</sup> Ga<sub>2</sub>O<sub>3</sub>,<sup>45</sup> and ZnO<sup>46</sup> that work under external bias work. Nevertheless, they are much better than other WBS UVPDs composed of nonpolar GaN,<sup>47</sup> Ni/GaN/

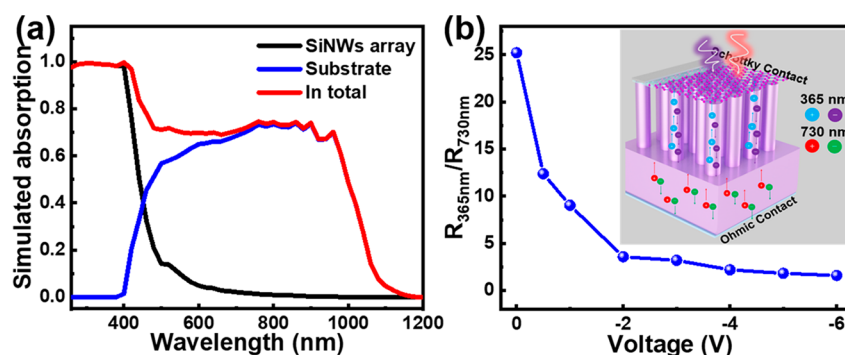


Figure 5. (a) Simulated absorption curve of SiNW array, Si substrate, and the in-total value. The simulation parameters are as follows:  $D = 45$  nm;  $L = 6.7$   $\mu\text{m}$ ;  $P = 100$  nm;  $\theta = 0^\circ$ ; Si substrate thickness of  $500$   $\mu\text{m}$ . (b) Rejection ratio as a function of different bias voltages. The inset shows a schematic diagram of the main distribution of photogenerated carriers generated under 365 and 730 nm light illumination.

Ti/Al,<sup>48</sup> and ZnO NW array/Spiro-MeOTAD<sup>49</sup> heterojunction structures. Notably, the present device is also characterized by relatively high responsivity and fast response speed which is better than commercial GaN UV photodetectors (GaN detector (GUA-S12SD in Gen UV)).

Another thing that should be pointed out is that, although the optical absorption in the UV region is due to the strong leaky mode resonance which is highly beneficial for UV light detection, it does not follow that the underlying Si mother wafer that supports the SiNW array cannot absorb any incident light. According to our simulation result shown in Figure 5a, the Si wafer exhibits broadband absorption in the region from 400 to 1000 nm, with peak absorption at approximately 900 nm, which is consistent with the experimental result (Figure S7). On this account, the photosensitivity at 730 nm illumination is unneglectable, leading to a relatively small rejection ratio ( $365\text{ nm}/730\text{ nm}$ ) of 25 at 0 V, in comparison with other conventional wide band gap semiconductor-based UVPDs.<sup>50</sup> In addition, such a rejection ratio will be further decreased to 2.1 as the device is applied by a large negative bias voltage of  $-6$  V (Figure 5b). This finding is reasonable considering the fact that the generation of photocurrent of the graphene/small diameter SiNW array UPVD is determined not only by the generation of electron-hole pairs but also by the corresponding separation efficiency of the built-in electric field. According to our calculation (see SI) and research in the relevant literature,<sup>51</sup> the width of the depletion region and diffusion length of carriers of UPVD are approximately 0.6 and  $\sim 1$   $\mu\text{m}$ , respectively. When illuminated by 365 and 730 nm light, the generation regions of electron-hole pairs are localized at the MLG/SiNW interface and in the substrate far from the depletion and diffusion region, respectively. Such a difference in the distribution of photogenerated carriers leads to higher separation efficiency of electron-hole pairs under 365 nm light than under 730 nm illumination. As a result, the photocurrent generated by 365 nm illumination at zero bias is at least 1 order of magnitude larger than that at 730 nm (Figure S8). However, the separation efficiency of the built-in electric field to the electron-hole pair will be substantially strengthened when the device is applied at a negative voltage, resulting in an increased rate of photocurrent under 730 nm illumination compared to that under 365 nm illumination due to the different regions generated by photogenerated carriers. Therefore, the rejection ratio ( $365\text{ nm}/730\text{ nm}$ ) is found to gradually decrease with increasing negative bias voltage.

## CONCLUSIONS

In summary, we have reported a non-WBS sensitive UVPD by using a SiNW array with a diameter of  $\sim 45$  nm as building blocks. The as-assembled MLG/SiNW array heterojunction is sensitive to UV illumination with a responsivity of  $0.151\text{ A/W}$  at 365 nm and a specific detectivity of  $1.37 \times 10^{12}$  Jones, respectively, which is comparable to other UVPDs made of conventional WBSs. In addition, it is insensitive to visible and NIR light under zero bias voltage with a rejection ratio ( $R_{365\text{ nm}}/R_{730\text{ nm}}$ ) of 25. Theoretical simulation based on FEM shows that this abnormal photoresponse in the UV region is related to the  $\text{HE}_{1\text{m}}$  leaky modes that can enable the shift of the peak absorption spectrum from the NIR to UV regions. These results show that narrow band gap semiconductor nanostructures are potential building blocks for the assembly of high-performance UVPDs in future optoelectronic devices and systems.

## EXPERIMENTAL SECTION

**Materials Synthesis and Characterization.** In this study, monolayer graphene (MLG) films were grown by a chemical vapor deposition (CVD) method, in which  $\text{CH}_4$  and  $\text{H}_2$  were used as reaction sources, and  $50\text{ }\mu\text{m}$  thick copper foil was used as the catalytic substrate. The SiNWs array was synthesized by an MCE approach. Briefly, a (100) oriented silicon wafer ( $n$ -type,  $\rho$ :  $1\text{--}10\text{ }\Omega\text{ cm}$ ) was ultrasonically cleaned in acetone, ethanol, and deionized water for 10 min, respectively, and then treated in boiling piranha solution (4:1 (v/v)  $\text{H}_2\text{SO}_4/\text{H}_2\text{O}_2$ ) for 1 h. The silicon surface coated with single-layer polystyrene (PS) spheres (Diameter = 100 nm, dispersion < 6%, 1:1 (v/v) solid content 2.5%: ethanol) through a self-assembly method was then treated by inductively coupled plasma (ICP-601) to form a non-close-packed pattern with a diameter of  $\sim 50$  nm. The RF power of the top and bottom electrodes was set to be 140 and 40 W, respectively. The pressure in the chamber was set at 5 m-torr, the flow rate of  $\text{O}_2$  was 50 standard cubic centimeter per minute (sccm), and the reaction time was 55 s. Afterward, the above sample was deposited with a Au layer ( $\sim 25$  nm) via ion sputtering and immersed in etching solution ( $\text{HF}:\text{H}_2\text{O}_2 = 4:1$  (v/v)) for 10 min. Finally, the as-obtained NWs were immersed in 5% HF solution for 5 min to passivate the surface. The morphology of PS spheres and SiNWs array was studied by scanning electron microscopy (SEM, SIRION 200 FEG). The crystal structure of the NWs was investigated using a FETEM instrument (JEOL JEM-2100F). The absorption spectra of the samples were measured by a UV-vis (NIR) spectrophotometer. The graphene was analyzed by Raman spectroscopy (JY, LabRAM HR800).

**Device Fabrication and Analysis.** To fabricate MLG/SiNWs array heterojunction UVPD, a square window is formed by covering tape on the vertical SiNWs array as an insulating layer. Then, the



MLG with poly(methyl methacrylate) (PMMA) was transferred to the surface of the SiNWs array. Finally, the silver paste was placed at the MLG surface where the PMMA was removed away by acetone. In-Ga alloy was pasted on the bottom part of the Si wafer for Ohmic contact. The electrical measurement was carried out on the semiconductor parameter test system (Keithley 4200-SCS), and spectral response was measured on a monochromator (LE-SP-M300). To study the photoresponse, laser diodes with different wavelengths (265, 365, 450, 530, 660, 730, 810, 970, and 1050 nm) were used as the illumination sources. Before the measurement, the power intensity of all light sources was carefully calibrated by the power meter (Thorlabs GmbH, PM100D).

**Numerical Simulation.** On the basis of the finite element method, all numerical simulations were performed using commercial software COMSOL Multiphysics 5.4. In the calculations, by setting periodic boundary conditions in  $x$  and  $y$  directions, an infinite number of SiNWs can be simulated by calculating the unit structure. Meanwhile, the incident light was set to be an  $x$ -polarized plane wave propagating along the  $z$ -axis. The top and bottom layers were defined as a perfectly matched layer (PML) with a thickness of 400 nm to absorb all the outgoing radiation. The refractive index of air was set to be 1. The silicon optical constants were obtained from the Sopra S. A. Company.

## ASSOCIATED CONTENT

### Supporting Information

The Supporting Information is available free of charge at <https://pubs.acs.org/doi/10.1021/acsnano.1c06705>.

$I$ – $V$  curve of the Ag/Graphene/Ag and the In-Ga/n-Si/In-Ga contact (Figure S1), SEM image of scraped SiNWs (Figure S2), Raman spectrum of the graphene film (Figure S3), solution of leaky modes, absorption curve of SiNWs array with different diameters (Figure S4), contour plot of the absorption (Figure S5), photoresponse curves of the MLG/SiNWs array heterojunction UVPD (Figure S6), solution of key parameters of the photodetector, experimental absorption spectra (Figure S7), solution of the width of depletion region,  $I$ – $V$  curves of 365 and 730 nm illumination (Figure S8) (PDF)

## AUTHOR INFORMATION

### Corresponding Authors

**Feng-Xia Liang** – School of Materials Science and Engineering and Anhui Provincial Key Laboratory of Advanced Functional Materials and Devices, Hefei University of Technology, Hefei 230009, China; [orcid.org/0000-0002-8237-3534](https://orcid.org/0000-0002-8237-3534); Email: [fxliang@hfut.edu.cn](mailto:fxliang@hfut.edu.cn)

**Lin-Bao Luo** – School of Electronic Science and Applied Physics, Hefei University of Technology, Hefei 230009, China; [orcid.org/0000-0001-8651-8764](https://orcid.org/0000-0001-8651-8764); Email: [luolb@hfut.edu.cn](mailto:luolb@hfut.edu.cn)

### Authors

**Jun-Jie Wang** – School of Electronic Science and Applied Physics, Hefei University of Technology, Hefei 230009, China

**Can Fu** – School of Electronic Science and Applied Physics, Hefei University of Technology, Hefei 230009, China

**Hai-Yang Cheng** – School of Electronic Science and Applied Physics, Hefei University of Technology, Hefei 230009, China

**Xiao-Wei Tong** – School of Electronic Science and Applied Physics, Hefei University of Technology, Hefei 230009, China

**Zhi-Xiang Zhang** – School of Electronic Science and Applied Physics, Hefei University of Technology, Hefei 230009, China

**Di Wu** – Key Laboratory of Materials Physics of Ministry of Education, Department of Physics and Engineering, Zhengzhou University, Zhengzhou 450052, China; [orcid.org/0000-0003-3266-0612](https://orcid.org/0000-0003-3266-0612)

**Li-Miao Chen** – Hunan Provincial Key Laboratory of Micro & Nano Materials Interface Science, College of Chemistry and Chemical Engineering, Central South University, Changsha 410083, China

Complete contact information is available at:

<https://pubs.acs.org/doi/10.1021/acsnano.1c06705>

### Author Contributions

J.-J.W., X.-W.T., and C.F. prepared the samples, collected and analyzed the data, simulated the device, and wrote the paper. L.-B.L. and F.-X.L. conceived the idea, supervised the whole project, analyzed the results, and wrote the paper. H.-Y.C. and D.W. helped with the study of the optical properties of the materials. L.-M.C. and Z.-X.Z. helped with the study of experimental results. All authors discussed the results and commented on the manuscript.

### Notes

The authors declare no competing financial interest.

## ACKNOWLEDGMENTS

This work was supported by the National Natural Science Foundation of China (NSFC, No. 62074048), the Fundamental Research Funds for the Central Universities (JZ2018-HGXC0001), the Funds for the Central Universities (JZ2018HGPB0275, PA2020GDKC0014), and the Open Foundation of Anhui Provincial Key Laboratory of Advanced Functional Materials and Devices (4500-411104/011).

## REFERENCES

- (1) Kang, C. H.; Dursun, I.; Liu, G.; Sinatra, L.; Sun, X.; Kong, M.; Pan, J.; Maity, P.; Ooi, E. N.; Ng, T. K.; Mohammed, O. F.; Bakr, O. M.; Ooi, B. S. High-Speed Colour-Converting Photodetector with All-Inorganic CsPbBr<sub>3</sub> Perovskite Nanocrystals for Ultraviolet Light Communication. *Light: Sci. Appl.* **2019**, *8*, 94.
- (2) Goossens, S.; Navickaite, G.; Monasterio, C.; Gupta, S.; Piqueras, J. J.; Pérez, R.; Burwell, G.; Nikitskiy, I.; Lasanta, T.; Galán, T.; Puma, E.; Centeno, A.; Pesquera, A.; Zurutuza, A.; Konstantatos, G.; Koppens, F. Broadband Image Sensor Array Based on Graphene-CMOS Integration. *Nat. Photonics* **2017**, *11*, 366–371.
- (3) Chen, Y. F.; Wang, Y.; Wang, Z.; Gu, Y.; Ye, Y.; Chai, X. L.; Ye, J. F.; Chen, Y.; Xie, R. Z.; Zhou, Y.; Hu, Z. G.; Li, Q.; Zhang, L. L.; Wang, F.; Wang, P.; Miao, J. S.; Wang, J. L.; Chen, X. S.; Lu, W.; Zhou, P.; Hu, W. D. Unipolar Barrier Photodetectors Based on van der Waals Heterostructures. *Nat. Electron.* **2021**, *4*, 357–363.
- (4) Xu, X. J.; Chen, J.; Cai, S.; Long, Z.; Zhang, Y.; Su, L.; He, S.; Tang, C.; Liu, P.; Peng, H. S.; Fang, X. S. A Real-Time Wearable UV-Radiation Monitor Based on a High-Performance p-CuZnS/N-TiO<sub>2</sub> Photodetector. *Adv. Mater.* **2018**, *30*, 1803165.
- (5) Cai, Q.; You, H. F.; Guo, H.; Wang, J.; Liu, B.; Xie, Z. L.; Chen, D. J.; Lu, H.; Zheng, Y. D.; Zhang, R. Progress on AlGaN-Based Solar-Blind Ultraviolet Photodetectors and Focal Plane Arrays. *Light: Sci. Appl.* **2021**, *10*, 94.
- (6) Qiu, M. J.; Sun, P.; Liu, Y. J.; Huang, Q. T.; Zhao, C. X.; Li, Z. H.; Mai, W. J. Visualized UV Photodetectors Based on Prussian Blue/TiO<sub>2</sub> for Smart Irradiation Monitoring Application. *Adv. Mater. Technol.* **2018**, *3*, 1700288.
- (7) Yang, T.; Chen, S. L.; Li, X. X.; Xu, X. J.; Gao, F. M.; Wang, L.; Chen, J. H.; Yang, W. Y.; Hou, X. M.; Fang, X. S. High-Performance SiC Nanobelt Photodetectors with Long-Term Stability against 300 °C up to 180 Days. *Adv. Funct. Mater.* **2019**, *29*, 1806250.

- (8) Gundimeda, A.; Krishna, S.; Aggarwal, N.; Sharma, A.; Sharma, N. D.; Maurya, K. K.; Husale, S.; Gupta, G. Fabrication of Non-Polar GaN Based Highly Responsive and Fast UV Photodetector. *Appl. Phys. Lett.* **2017**, *110*, 103507.
- (9) Soci, C.; Zhang, A.; Xiang, B.; Dayeh, S. A.; Aplin, D.; Park, J.; Bao, X.; Lo, Y. H.; Wang, D. ZnO Nanowire UV Photodetectors with High Internal Gain. *Nano Lett.* **2007**, *7*, 1003–1009.
- (10) Kong, W. Y.; Wu, G. A.; Wang, K. Y.; Zhang, T. F.; Zou, Y. F.; Wang, D. D.; Luo, L. B. Graphene- $\beta$ -Ga<sub>2</sub>O<sub>3</sub> Heterojunction for Highly Sensitive Deep UV Photodetector Application. *Adv. Mater.* **2016**, *28*, 10725–10731.
- (11) Zhao, B.; Wang, F.; Chen, H. Y.; Wang, Y. P.; Jiang, M. M.; Fang, X. S.; Zhao, D. X. Solar-Blind Avalanche Photodetector Based on Single ZnO-Ga<sub>2</sub>O<sub>3</sub> Core-Shell Microwire. *Nano Lett.* **2015**, *15*, 3988–3993.
- (12) Monroy, E.; Omnès, F.; Calle, F. Wide-Bandgap Semiconductor Ultraviolet Photodetectors. *Semicond. Sci. Technol.* **2003**, *18*, R33–R51.
- (13) Hobgood, H. M.; Glass, R. C.; Augustine, G.; Hopkins, R. H.; Jenny, J.; Skowronski, M.; Mitchel, W. C.; Roth, M. Semi-Insulating 6H-SiC Grown by Physical Vapor Transport. *Appl. Phys. Lett.* **1995**, *66*, 1364–1366.
- (14) Bonef, B.; Cramer, R.; Speck, J. S. Nanometer Scale Composition Study of MBE Grown BGaN Performed by Atom Probe Tomography. *J. Appl. Phys.* **2017**, *121*, 225701.
- (15) Tan, S. T.; Chen, B. J.; Sun, X. W.; Fan, W. J.; Kwok, H. S.; Zhang, X. H.; Chua, S. J. Blueshift of Optical Band Gap in ZnO Thin Films Grown by Metal-Organic Chemical-Vapor Deposition. *J. Appl. Phys.* **2005**, *98*, 013505.
- (16) Xi, Y. A.; Chen, K. X.; Mont, F.; Kim, J. K.; Wetzel, C.; Schubert, E. F.; Liu, W.; Li, X.; Smart, J. A. Very High Quality AlN Grown on (0001) Sapphire by Metal-Organic Vapor Phase Epitaxy. *Appl. Phys. Lett.* **2006**, *89*, 103106.
- (17) Xie, C.; Lu, X. T.; Tong, X. W.; Zhang, Z. X.; Liang, F. X.; Liang, L.; Luo, L. B.; Wu, Y. C. Recent Progress in Solar-Blind Deep-Ultraviolet Photodetectors Based on Inorganic Ultrawide Bandgap Semiconductors. *Adv. Funct. Mater.* **2019**, *29*, 1806006.
- (18) Ajiki, Y.; Kan, T.; Yahiro, M.; Hamada, A.; Adachi, J.; Adachi, C.; Matsumoto, K.; Shimoyama, I. Silicon Based Near Infrared Photodetector Using Self-Assembled Organic Crystalline Nano-Pillars. *Appl. Phys. Lett.* **2016**, *108*, 151102.
- (19) Wan, X.; Xu, Y.; Guo, H. W.; Shehzad, K.; Ali, A.; Liu, Y.; Yang, J. Y.; Dai, D. X.; Lin, C. T.; Liu, L. W.; Cheng, H. C.; Wang, F. Q.; Wang, X. M.; Lu, H.; Hu, W. D.; Pi, X. D.; Dan, Y. P.; Luo, J. K.; Hasan, T.; Duan, X. F.; et al. A Self-Powered High-Performance Graphene/Silicon Ultraviolet Photodetector with Ultra-Shallow Junction: Breaking the Limit of Silicon? *npj 2D Mater. Appl.* **2017**, *1*, 4.
- (20) Shi, L.; Nihtianov, S. Comparative Study of Silicon-Based Ultraviolet Photodetectors. *IEEE Sens. J.* **2012**, *12*, 2453–2459.
- (21) Mokkapat, S.; Saxena, D.; Tan, H. H.; Jagadish, C. Optical Design of Nanowire Absorbers for Wavelength Selective Photodetectors. *Sci. Rep.* **2015**, *5*, 15339.
- (22) Fountaine, K. T.; Whitney, W. S.; Atwater, H. A. Resonant Absorption in Semiconductor Nanowires and Nanowire Arrays: Relating Leaky Waveguide Modes to Bloch Photonic Crystal Modes. *J. Appl. Phys.* **2014**, *116*, 153106.
- (23) Cao, L. Y.; White, J. S.; Park, J. S.; Schuller, J. A.; Clemens, B. M.; Brongersma, M. L. Engineering Light Absorption in Semiconductor Nanowire Devices. *Nat. Mater.* **2009**, *8*, 643–647.
- (24) Wang, B.; Leu, P. W. Tunable and Selective Resonant Absorption in Vertical Nanowires. *Opt. Lett.* **2012**, *37*, 3756–3758.
- (25) Huang, Z.; Fang, H.; Zhu, J. Fabrication of Silicon Nanowire Arrays with Controlled Diameter, Length, and Density. *Adv. Mater.* **2007**, *19*, 744–748.
- (26) Yu, J.; Yan, Q.; Shen, D. Co-Self-Assembly of Binary Colloidal Crystals at the Air-Water Interface. *ACS Appl. Mater. Interfaces* **2010**, *2*, 1922–1926.
- (27) Wu, C. Y.; Wang, Z.; Liang, L.; Gui, T.; Zhong, W.; Du, R. C.; Xie, C.; Wang, L.; Luo, L. B. Graphene-Assisted Growth of Patterned Perovskite Films for Sensitive Light Detector and Optical Image Sensor Application. *Small* **2019**, *15*, 1900730.
- (28) Seo, K.; Wober, M.; Steinvurzel, P.; Schonbrun, E.; Dan, Y.; Ellenbogen, T.; Crozier, K. B. Multicolored Vertical Silicon Nanowires. *Nano Lett.* **2011**, *11*, 1851–1856.
- (29) Wang, B.; Leu, P. W. Enhanced Absorption in Silicon Nanowire Arrays for Photovoltaics. *Nanotechnology* **2012**, *23*, 194003.
- (30) Wang, X.; Cheng, Z.; Xu, K.; Tsang, H. K.; Xu, J. B. High-Responsivity Graphene/Silicon-Heterostructure Waveguide Photodetectors. *Nat. Photonics* **2013**, *7*, 888–891.
- (31) Park, H.; Crozier, K. B. Vertically Stacked Photodetector Devices Containing Silicon Nanowires with Engineered Absorption Spectra. *ACS Photonics* **2015**, *2*, 544–549.
- (32) Um, H. D.; Solanki, A.; Jayaraman, A.; Gordon, R. G.; Habbal, F. Electrostatically Doped Silicon Nanowire Arrays for Multispectral Photodetectors. *ACS Nano* **2019**, *13*, 11717–11725.
- (33) Di Bartolomeo, A. Graphene Schottky Diodes: An Experimental Review of the Rectifying Graphene/Semiconductor Heterojunction. *Phys. Rep.* **2016**, *606*, 1–58.
- (34) Miao, X.; Tongay, S.; Petterson, M. K.; Berke, K.; Rinzler, A. G.; Appleton, B. R.; Hebard, A. F. High Efficiency Graphene Solar Cells by Chemical Doping. *Nano Lett.* **2012**, *12*, 2745–2750.
- (35) Ryu, S.; Liu, L.; Berciaud, S.; Yu, Y.-J.; Liu, H.; Kim, P.; Flynn, G. W.; Brus, L. E. Atmospheric Oxygen Binding and Hole Doping in Deformed Graphene on a SiO<sub>2</sub> Substrate. *Nano Lett.* **2010**, *10*, 4944–4951.
- (36) Nusir, A. I.; Bauman, S. J.; Marie, M. S.; Herzog, J. B.; Manasreh, M. O. Silicon Nanowires to Enhance the Performance of Self-Powered Near-Infrared Photodetectors with Asymmetrical Schottky Contacts. *Appl. Phys. Lett.* **2017**, *111*, 171103.
- (37) Luo, L. B.; Zeng, L. H.; Xie, C.; Yu, Y. Q.; Liang, F. X.; Wu, C. Y.; Wang, L.; Hu, J. G. Light Trapping and Surface Plasmon Enhanced High-Performance NIR Photodetector. *Sci. Rep.* **2015**, *4*, 3914.
- (38) Kim, K.; Yoon, S.; Seo, M.; Lee, S.; Cho, H.; Meyyappan, M.; Baek, C. K. Whispering Gallery Modes Enhance the Near-Infrared Photoresponse of Hourglass-Shaped Silicon Nanowire Photodiodes. *Nat. Electron.* **2019**, *2*, 572–579.
- (39) Reddy, Y. A. K.; Ajitha, B.; Sreedhar, A.; Varrla, E. Enhanced UV Photodetector Performance in Bi-Layer TiO<sub>2</sub>/WO<sub>3</sub> Sputtered Films. *Appl. Surf. Sci.* **2019**, *494*, 575–582.
- (40) Fu, Q.-M.; Peng, J.-L.; Yao, Z.-C.; Zhao, H.-Y.; Ma, Z.-B.; Tao, H.; Tu, Y.-F.; Tian, Y.; Zhou, D.; Han, Y.-B. Highly Sensitive Ultraviolet Photodetectors Based on ZnO/SnO<sub>2</sub> Core-Shell Nanorod Arrays. *Appl. Surf. Sci.* **2020**, *527*, 146923.
- (41) Yadav, P. K.; Reddy, Y. A. K.; Ajitha, B.; Reddy, V. R. M. Oxygen Partial Pressure Dependent UV Photodetector Performance of WO<sub>3</sub> Sputtered Thin Films. *J. Alloys Compd.* **2020**, *816*, 152565.
- (42) Yadav, P. V. K.; Ajitha, B.; Reddy, Y. A. K.; Reddy, V. R. M.; Reddeppa, M.; Kim, M.-D. Effect of Sputter Pressure on UV Photodetector Performance of WO<sub>3</sub> Thin Films. *Appl. Surf. Sci.* **2021**, *536*, 147947.
- (43) Yadav, P. K.; Ajitha, B.; Kumar Reddy, Y. A.; Minnam Reddy, V. R. Enhanced Performance of WO<sub>3</sub> Photodetectors through Hybrid Graphene-Layer Integration. *ACS Appl. Electron. Mater.* **2021**, *3*, 2056–2066.
- (44) Yadav, P. K.; Ajitha, B.; Annapureddy, V.; Reddy, Y. A. K.; Sreedhar, A. Improved UV Photodetector Performance of NiO Films by Substitutional Incorporation of Li. *Mater. Lett.* **2021**, *301*, 130296.
- (45) Zhong, M.; Wei, Z.; Meng, X.; Wu, F.; Li, J. High-Performance Single Crystalline UV Photodetectors of  $\beta$ -Ga<sub>2</sub>O<sub>3</sub>. *J. Alloys Compd.* **2015**, *619*, 572–575.
- (46) Shaikh, S. K.; Inamdar, S. I.; Ganbavle, V. V.; Rajpure, K. Y. Chemical Bath Deposited ZnO Thin Film Based UV Photoconductive Detector. *J. Alloys Compd.* **2016**, *664*, 242–249.
- (47) Gundimeda, A.; Krishna, S.; Aggarwal, N.; Sharma, A.; Sharma, N. D.; Maurya, K.; Husale, S.; Gupta, G. Fabrication of Non-Polar



GaN Based Highly Responsive and Fast UV Photodetector. *Appl. Phys. Lett.* **2017**, *110*, 103507.

(48) Sun, X.; Li, D.; Li, Z.; Song, H.; Jiang, H.; Chen, Y.; Miao, G.; Zhang, Z. High Spectral Response of Self-Driven GaN-Based Detectors by Controlling the Contact Barrier Height. *Sci. Rep.* **2015**, *5*, 16819.

(49) Game, O.; Singh, U.; Kumari, T.; Banpurkar, A.; Ogale, S. ZnO (N)-Spiro-MeOTAD Hybrid Photodiode: An Efficient Self-Powered Fast-Response UV (Visible) Photosensor. *Nanoscale* **2014**, *6*, 503–513.

(50) Hatch, S. M.; Briscoe, J.; Dunn, S. A Self-Powered ZnO-Nanorod/CuSCN UV Photodetector Exhibiting Rapid Response. *Adv. Mater.* **2013**, *25*, 867–871.

(51) Dan, Y.; Seo, K.; Takei, K.; Meza, J. H.; Javey, A.; Crozier, K. B. Dramatic Reduction of Surface Recombination by *in Situ* Surface Passivation of Silicon Nanowires. *Nano Lett.* **2011**, *11*, 2527–2532.